Dual grain size-effects on hydrogen-assisted fatigue crack growth in 1 GPa-class medium-carbon martensitic steel

Yuhei Ogawa [a], Kazuhiro Kuriyama [b], Motomichi Koyama [c]

a *Research Center for Structural Materials, National Institute for Materials Science (NIMS), 1-2-1 Sengen, Tsukuba, 305-0047, Japan*
b *Graduate School of Engineering, Kyushu University, 744 Motooka, Nishi-ku, Fukuoka 819-0395, Japan*
c *Institute for Materials Research, Tohoku University, Katahira 2-1-1, Aoba-Ku, Sendai, Miyagi, 980-8577, Japan*

Corresponding author: Yuhei Ogawa
Email: OGAWA.yuhei@nims.go.jp

Abstract

The influence of prior austenite grain (PAG) size ranging from 6 to 90 μm on the fatigue crack growth (FCG) of a tempered 0.41%C lath martensitic steel was investigated in a 90 MPa H_2 gas environment at ambient temperature. Under the presence of H, severe FCG accelerations accompanying intergranular (IG) cracking along PAG boundaries as well as quasi-cleavage (QC) fracture along martensite block boundaries and {011} crystallographic planes were systematically found. Smaller PAG mitigated the acceleration at a relatively high-stress intensity *via* suppressing IG cracking. However, PAG refinement instead escalated the acceleration at a low-stress intensity factor where QC facture prevailed. This inverse grain size effect was discussed in terms of the plasticity criterion in triggering QC and its possible dependence on the microstructural length scale.

Keywords: hydrogen embrittlement; fatigue; fracture; martensitic steels; grain size

1. Introduction

Medium-carbon martensitic steels are vital pieces constituting the pressure vessels for the storage of hydrogen (H) gas, albeit a concern for their robustness is the mechanical degradation under H absorption: hydrogen embrittlement (HE) [1–6]. The experimental data in high-pressure H_2 gas uncovered that the detrimental H-effect manifests particularly as accelerated fatigue crack growth (FCG) [7–10], an extent of which escalates when the tensile strength exceeds 1 GPa. Improvement in the resistance to H-

assisted FCG is earnestly desired to realize a more significant economic efficiency with sufficient reliability.

The mechanical properties of martensitic steels depend essentially on their internal microstructures [11–15]. The microstructure of medium-carbon martensite exhibits a complex hierarchical framework comprising lath, block, packet, and prior austenite grains (PAG) [15,16]. PAG is the most controllable unit by changing the austenizing temperature [17]. A refinement of PAG simultaneously leads to the shrinkages of block and packet [18,19], suppressing the low-temperature ductile-to-brittle transition [14,20] and enhancing the resistance against temper embrittlement [21]. Moreover, the reduction in PAG size mitigates H-induced degradations in conventional tensile tests [22–24]. This beneficial outcome has been understood as a diminished damage accumulation in the proximity of PAG boundaries and resultant inhibition of intergranular fracture [22,23], a standard failure mode in the HE of high-strength steels [1,3,5].

Nevertheless, how those microstructural features influence the propagation of H-assisted cracks is still elusive. Contrary to the general propensities, a slower crack growth rate was reported for coarser PAGs in the delayed fracture experiments under static loading [25,26]. Unlike the tensile tests where deformation is uniform, the criteria for crack propagation rely on concentrated stress/strain inside the crack-tip zone, a dimension of which is equivalent to or smaller than the microstructural length scales. An inherently localized nature of fracture makes the linkage between PAG, packet, or block sizes and fracture resistance not straightforward. Specifically, the situation is intricate for FCG, wherein the loading is dynamic, and the crack-tip volume suffers from cyclic straining and transient damaging.

H-assisted FCG in steels under gaseous H_2 has been interpreted in terms of mechanistic and environmental variables involving strength level [7,8,27], stress intensity [7,8,28], load ratio [29], frequency [7,28], gas pressures [28,30], and temperature [31,32]. However, the microstructural impact was left behind the attention despite its significance as one of the keys to improving material performance. The present study tackles this problem as a pioneering work to elucidate the influence of PAG size on the FCG rate of 1GPa-class martensitic steel in a pressurized gaseous H_2 environment. The underlying rationale controlling the microstructure-dependent FCG is discussed based on the fractographic features and crack path morphologies.

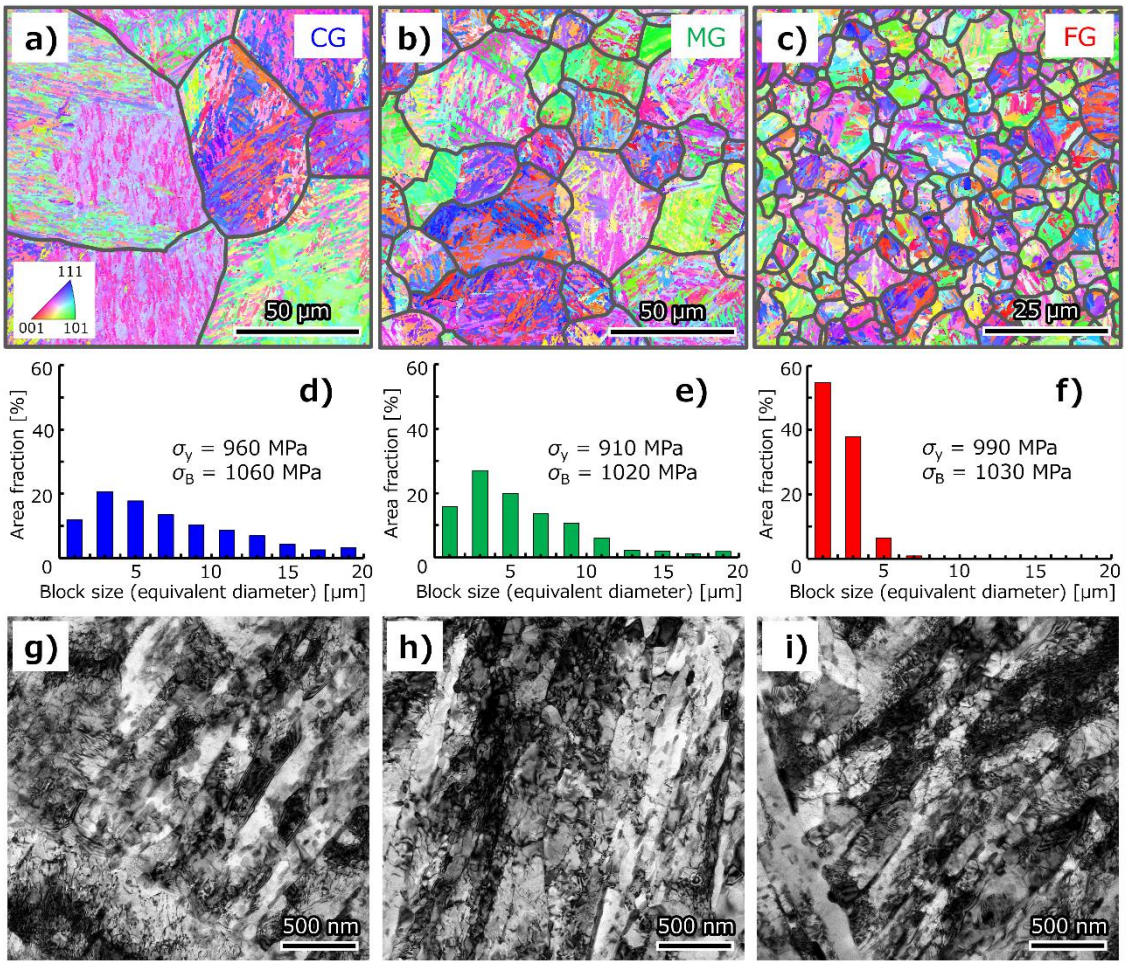

Fig. 1 Microstructures of the present steel with different PAG sizes, *i.e.*, CG, MG, and FG with the PAG sizes of 90, 40, and 6 μm, respectively, captured by (a)~(c) EBSD and (g)~(i) TEM. The gray lines in (a)~(c) delineate PAG boundaries involving the segments of 22~47° misorientations. (d)~(f) present the charts of block size automatically calculated from the EBSD software in the form of equivalent diameter. The yield stress, σ_y, and tensile strength, σ_B, of each material are indicated in (d)~(f).

2. Material and Methods

A steel with the composition of 0.41C-0.2Si-0.61Mn-0.014P-0.003S-0.1Cu-0.06Ni-1.02Cr-0.17Mo (mass%) was used. A 7 mm-thick plate was austenized at 1373 or 1173 K for 3600 s, followed by oil-quenching. A finer PAG sample was prepared by thermal cycling [33–35] at 1073 K: the plate was austenized at 1073 K for 3600 s, then oil-quenched; afterward, immersion into 1073 K salt bath for 300 s, and subsequent oil cooling were repeated five times. The samples treated at 1373, 1173, and 1073 K are designated as coarse grain (CG), medium grain (MG), and fine grain (FG). All samples were finally tempered at 873 K for 3600 s to adjust their tensile strength to around 1 GPa.

Compact tension (CT) specimens were fabricated from the longitudinal-transverse

orientation, the thickness and width of which were 6 and 26.4 mm. FCG tests were performed following ASTM-E647 [36] with a load ratio R = 0.1, using crack length measurement by unloading elastic compliance. The test environments were air and 90 MPa H_2 gas, both at 298 K, the loading frequencies for which were f = 5 and 1 Hz, respectively. The microstructures of heat-treated samples were characterized by electron backscattering diffraction (EBSD) and transmission electron microscope (TEM). A JEOL JSM-7001F scanning electron microscope (SEM) was used at 15 kV, and JEOL JEM-2100 TEM operated at 200 kV was employed after preparing 3 mm disks, the central parts of which were thinned *via* twin-jet electrochemical polishing. For the post-FCG specimen, the fracture surface and microstructural features adjacent to the mid-thickness crack path were analyzed as for the method in the author's previous studies [7,37].

3. Results and Discussion

Fig. 1 (a)~(f) present EBSD images of the microstructures after heat treatments and area fraction charts of block sizes when the minimum misorientation for boundary detection was 10˚. Martensite variants belonging to an identical PAG have misorientations out of 22~47˚ range [16]. Thus, most PAG boundaries can be identified if the boundaries include some segments with misorientations within 22~47˚, as delineated by gray lines in Fig. 1 (a)~(c). All materials were composed of a fully martensitic phase with average PAG sizes of 90, 40, and 6 μm for CG, MG, and FG, respectively, measured as average line intercept length. Note that the present approach overlooks small fractions of PAG boundaries, all the segments of which are out of 22~47˚, indicating that the measured PAG sizes were slightly overestimated. The block size also decreased with the shrinkage of PAG. TEM images in Fig. 1 (g)~(i) showcase the martensite laths with a thickness of 200~300 nm, wherein cementite precipitates are found along lath boundaries. No meaningful difference in lath morphology was recognized between the three samples. The yield strength, σ_y, and tensile strength, σ_B, measured in air at 298 K, are indicated in Fig. 1 (d)~(f). The σ_B of CG was slightly higher than those in MG and FG. A plausible reason for this anomaly is discussed in Supplementally Material. Nevertheless, σ_B close to 1 GPa was unalterably obtained, justifying their suitability for evaluating the PAG size dependence of H-assisted FCG under a fixed strength level.

Fig. 2 (a) showcases the relationship between FCG rate, da/dN, and stress intensity factor range, ΔK, in air and 90 MPa H_2. The microstructural variation did not affect the FCG rate in air, whereas a substantial impact was discovered in the case of H_2. Although all three materials exhibited an accelerated FCG in H_2 with respect to in-air, its magnitude became lesser as the reduction in PAG size at the ΔK above 20 MPa·m$^{1/2}$. The grain refinement effect mitigating the FCG acceleration is qualitatively consistent with the ordinary results of tensile tests [22–24] that smaller grain size leads to better HE resistance. However, an inverse grain size dependence emerged at ΔK below 20 MPa·m$^{1/2}$. That is, the materials with coarser PAGs expressed lower acceleration and superior resistance to H-assisted FCG. These tendencies can more straightforwardly be recognized in Fig. 2 (b), wherein Fig. 2 (a) was converted into the form of FCG rates in H_2 normalized by those in air, $(\mathrm{d}a/\mathrm{d}N)_{\mathrm{H}}/(\mathrm{d}a/\mathrm{d}N)_{\mathrm{Air}}$.

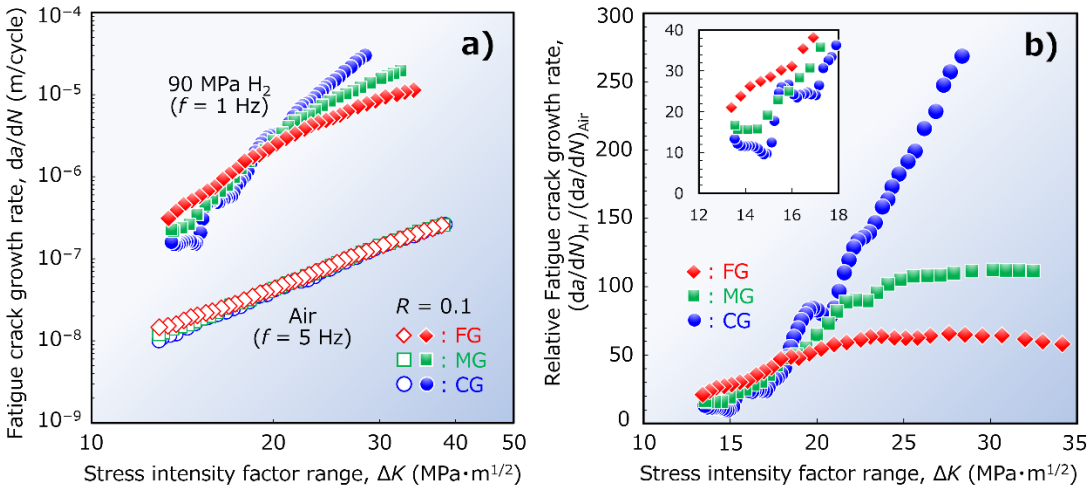

Fig. 2 (a) FCG rate per cycle, da/dN, versus ΔK of the JIS-SCM440 steel with different PAG sizes in air and 90 MPa H_2 gas. (b) reconstructs (a) in the form of relative FCG rates in H_2 concerning those in air. The inset in (b) magnifies the low ΔK regime where inverse grain size dependence was observed.

The fracture surfaces in the two ΔK regimes, where standard and inverse grain size dependences were found (*i.e.*, ΔK > 20 MPa·m$^{1/2}$ and < 20 MPa·m$^{1/2}$), are shown in Fig. 3. Intergranular (IG) and faceted quasi-cleavage (QC) fractures were mixedly captured in H_2 irrespective of PAG size, while all materials displayed ductile transgranular feature including fatigue striations in air. The IG regions seemed smooth at low magnification (Fig. 3 (a)~(d)), although their surface was decorated with nano-scale undulations (Fig. 3

(e)). Meanwhile, the QCs exhibited lath-like features accompanying fine steps and ridges (Fig. 3 (e)), with the entire scaling of each facet being equivalent to PAG size. These distinctions enabled one to distinguish IGs from QCs. The area fraction of IG was a positive function of both ΔK and PAG size (Fig. 3 (f)), implicating greater importance of IG than QC in triggering FCG acceleration as the increases of those mechanistic and microstructural variables.

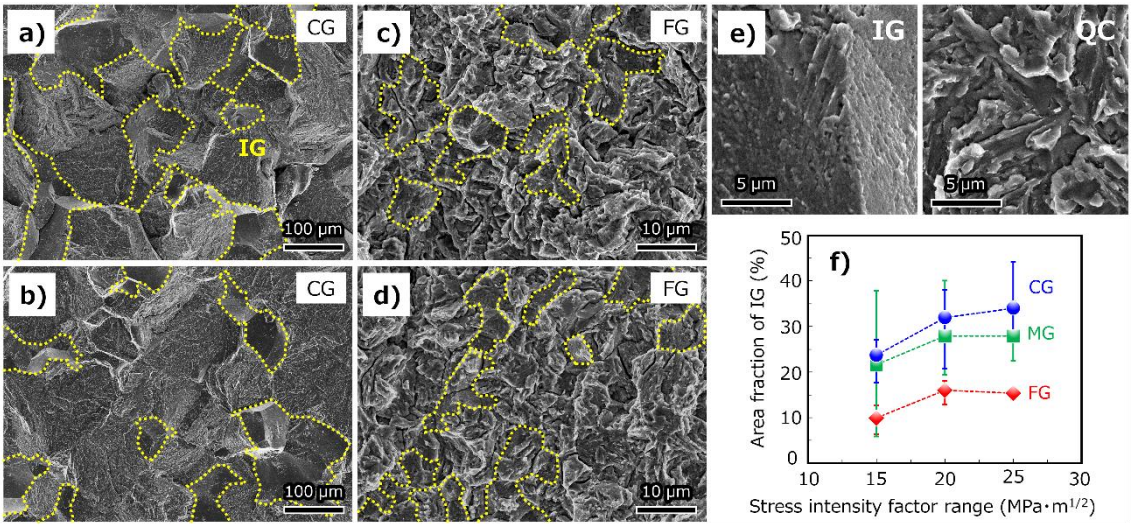

Fig. 3 Fracture surfaces of the mid-thickness positions of (a)(b) CG and (c)(d) FG in 90 MPa H_2 at (a)(c) ΔK = 25 MPa·m$^{1/2}$ and (b)(d) 15 MPa·m$^{1/2}$. The crack growth direction is from top to bottom in each picture. The details of IG and QC in CG at ΔK = 15 MPa·m$^{1/2}$ are shown in (e). (f) summarizes the IG area fraction versus ΔK, obtained from three field-of-views involving the central thickness and ±1 mm apart from the center.

Fig. 4 (a)~(c) present EBSD images on the crack cross-sections at ΔK = 25 MPa·m$^{1/2}$ in H_2. In CG (Fig. 4 (a)), a major part of the crack path traced PAG boundaries involving 22~47° misorientations [16], reflecting IGs observed in Fig. 3 (a). Note that the fraction of PAG (IG) fracture on the cross-section was larger than that on the fracture surface, possibly due to missing counts of several IG parts with intricate surface features [38,39]. With a reduction in the PAG size, the result in Fig. 3 (f) was reproduced as a decreasing fraction of the PAG boundary cracking (Fig. 4 (c)). Instead, the cracks partially selected block boundaries or transgranular paths. Some parts of the crack paths could not be specified because of their configurational complexity. Another noteworthy fact in Fig. 4 (a)~(c) was that, when the crack encounters PAG boundaries nearly perpendicular to its growth direction or PAG triple junctions, it showed temporal branching/deflection or

blunting (marked by black arrows). The frequency of such events was greater in FG, where the density of PAG boundaries was highest.

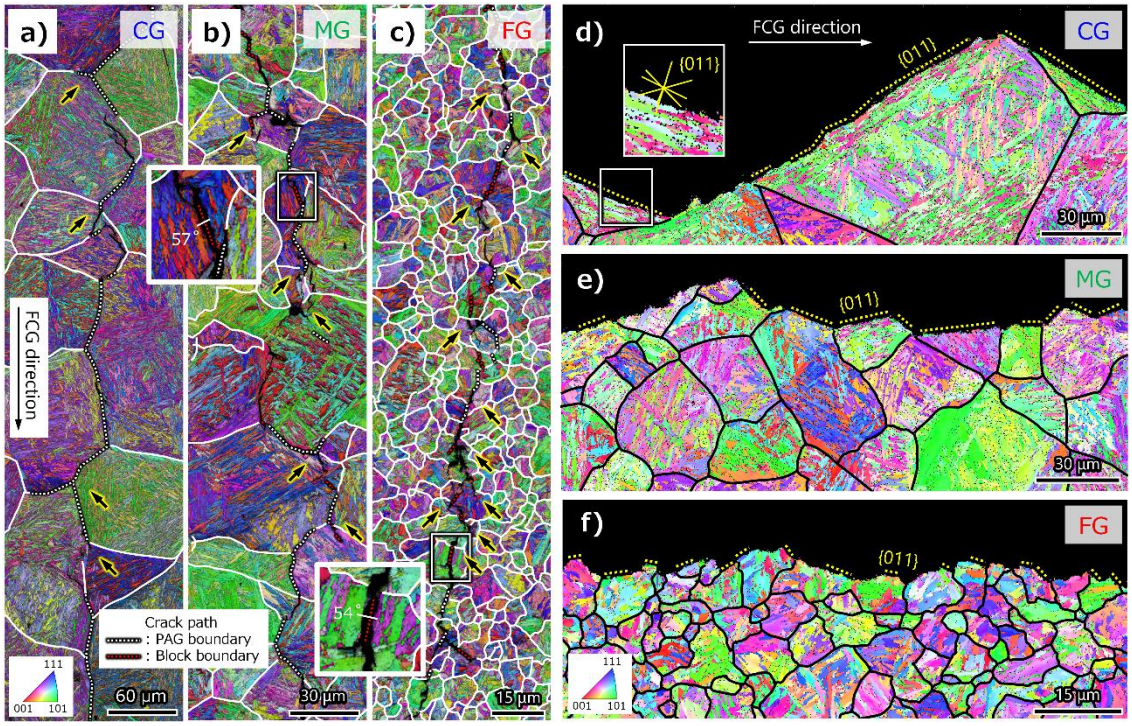

Fig. 4 EBSD inverse pole figure maps around the mid-thickness fracture paths in (a)(d) CG, (b)(e) MG, and (c)(f) FG at (a)~(c) ΔK = 25 MPa·m$^{1/2}$ and (d)~(f) 15 MPa·m$^{1/2}$. The fracture surfaces in (d)~(f) were Ni-plated before polishing. The white and black solid lines delineate PAG boundaries involving the segments with 22~47° misorientations. Some locations where crack exhibited branching/deflection or blunting are marked with arrows. The regions surrounded by rectangles are magnified in the insets.

The EBSD maps beneath the fracture surface at ΔK = 15 MPa·m$^{1/2}$ are exhibited in Fig. 4 (d)~(e). Unlike ΔK = 25 MPa·m$^{1/2}$, the cracks consisted of grain size-scale straight segments, each insistently along {011} crystallographic planes as judged by two-dimensional trace analysis. The coincidence between these {011} segments and grain size, as well as their straight shape, infer that they express the lateral views of QC facets observed in Fig. 3. Potentially, these reflect the fractures along transgranular {011} planes or block boundaries having {011} habit planes, albeit the lack of mating halves restricted an exact specification of the microstructural crack path. Individual {011} segments tended to lay parallel to the longitudinal axis of martensite blocks, mainly when the PAG size was large. Accordingly, the cracks exhibited winding configurations with the wavelength equivalent to the microstructural scaling. Note that these analyses were

performed in a size scale of martensite blocks. In a finer length scale, individual martensite laths in a block mutually have small misorientations below the angular resolution of EBSD, which is considered merely as measurement errors here.

The correlations between the pathways of H-assisted cracks and lath martensitic microstructure was elaborated by Chen et al. [39–41]. PAG boundary, where the atomic bond is weakened by segregated impurities [1,21] and H [42–44], becomes a selective fracture pathway in the material with σ_B > 1 GPa, when the boundary lies almost perpendicular to the loading axis. The development of internal stress and deformation-assisted H segregation due to strain incompatibility and crystal discontinuity between the neighboring grains further aids the boundary decohesion [1,3,41,43,45–47]. Accumulation or pile-up of dislocations at the boundary proximity gives rise to stress concentration and transport matrix H into the boundary [43,45–47], an instance should be promoted under coarser PAG and block because the mean free path for dislocations becomes longer (*i.e.*, number of pile-up dislocations increases with increasing grain size). Momotani et al. directly demonstrated such dislocation-driven H segregation along PAG boundaries, even at a small strain with no macroscale plasticity [48]. Additionally, a more serious HE-susceptibility under higher initial dislocation density [23], as for the case of the dislocations introduced *via* plastic deformation, evidences the importance of dislocation-mediated processes for fracture. However, high-angle grain boundaries, including PAG and block boundaries perpendicular to the crack, and triple junctions of PAGs resist the crack propagation, arresting it *via* provoking temporal branching or blunting [39–41,49]. The present crack propagation behavior under high ΔK (Fig. 4 (a)~(c)) was well consistent with these studies, even though the loading mode was static in [39,40]. Considering the perspectives above, the superior resistance to H-assisted FCG in finer PAG material is now understood straightforwardly. Namely, FCG slows down by the grain refinement since the developments of H segregation and internal stress are weakened; besides, the crack more often encounters obstacle boundaries. The latter may be prominent at high ΔK with the FCG rate of 10^{-5} μm/cycle order (Fig. 2 (a)), wherein the frequency of encountering the resistances out of a given number of load cycles is greater. Moreover, a partitioning and low concentration of other embrittling elements, *i.e.*, P and S, per PAG area could act as an additional IG diminisher.

In contrast, sub-micron orders of da/dN at low ΔK (Fig. 2 (a)) mean that the crack

encounters obstacle PAG boundaries merely per several tens to a few hundreds of cycles from a two-dimensional viewpoint. This lesser chance of encountering PAGs is probably one of the reasons for the diminished benefit of PAG refinement. Rather, refinement of PAG augmented the FCG rate in H_2, demonstrating its detriment at $\Delta K < 20$ MPa·m$^{1/2}$. The slower FCG rate in coarser PAG is superficially ascribed to the reduction in effective stress intensity [50] or crack closure [51] due to undulated crack shape and fracture surface roughness (Fig. 4 (d)~(f)). Nevertheless, these geometrical factors can be ruled out (see Supplementally Material); thereby, the outcome is an intrinsic impact of the difference in the microstructure.

The key to understanding the low ΔK behavior was QC, possibly along block boundaries and {011} planes (Fig. 3 and Fig. 4). As for IG, QC is a common feature in the HE of martensite, in which more intense plasticity has been believed as its prerequisite [41,52,53]. Based on their highly misoriented nature around 60° [16] and resultant large strain incompatibility, the block boundary fracture was linked to local strain-hardening in the boundary proximity, elevating the stress toward the critical boundary decohesion level, which may also be reduced by H [42–44]. Meanwhile, {011} plane failure was attributed to glide plane decohesion *via* preferential in-plane slip and subsequent planar accumulation of lattice defects [52–55]. In the latter context, the fracture along the longitudinal axis of the block (Fig. 4 (d)~(f)) can reasonably be understood since a large mean free path for dislocations there induces a prevalence of slip activity [56]. Whatever the predominant mechanisms, the most crucial criterion for the onset of these events is supposedly dislocation density, a parameter inversely proportional to the dislocation mean free path under a given plastic strain [57,58].

For the present material, the crack-tip plastic zone size, r_p, at $\Delta K = 15$ MPa·m$^{1/2}$ under plane strain condition (*i.e.*, mid-thickness of CT specimen) is around 30 μm if one uses Irwin's approximation (*i.e.*, $r_p = (1/3\pi)(K_{max}/\sigma_y)^2$, where K_{max} is the maximum stress intensity factor) [59]. The value is two orders of magnitude larger than the relevant average FCG rate in H_2 (Fig. 2 (a)), indicating that hundreds of cycles are required for the crack to pass through the pre-existing plastic zone ahead of it. Through this penetrating process, the volume surrounding the crack front suffers from repeated plastic straining [60], during which dislocations gradually accumulate near martensitic boundaries and on transgranular {011} planes. Once the dislocation density or strain-hardening rises

sufficiently, crack propagation along those specific paths close to the crack-tip ultimately commences. Essentially, such a critical condition could more readily be achieved in a finer PAG material because of its shorter dislocation mean free path and faster dislocation accumulation rate [57,58]. That is, owing to this plasticity-controlled nature of crack propagation at low ΔK, the fracture requirement is satisfied with fewer strain cycles in FG, leading to a more accelerated FCG in H_2 than CG and MG.

4. Conclusion

The influence of PAG size on the FCG of 1 GPa-class medium-carbon lath martensitic steel was investigated in 90 MPa H_2 gas. FCG rate was unalterably accelerated under the presence of H, although refinement of PAG from 90 to 6 μm mitigated the magnitude of acceleration under ΔK above 20 MPa·m$^{1/2}$ *via* suppression of IG fracture. However, smaller PAG resulted in a more significant acceleration at a smaller ΔK domain, wherein QC fracture along block boundaries and {011} planes prevailed. This inverse grain size dependence was ascribed to the plasticity-controlled nature of QC, a failure mode requiring critical dislocation density, which might more readily be satisfied with a lesser number of cyclic strain when the microstructural length scales are smaller.

Acknowledgment

This work was financially supported by The Hattori Hokokai Foundation, Japan. Y.O. is also grateful to Dr. Kaneaki Tsuzaki for his valuable comments for preparing the material used in this study, as well as to Research Center for Hydrogen Industrial Use and Storage (HYDROGENIUS) in Kyushu University for the experimental support.

References

[1] McMahon CJ. Hydrogen-induced intergranular fracture of steels. Eng Fract Mech 2001;68:773–88. https://doi.org/10.1016/S0013-7944(00)00124-7.

[2] Bhadeshia HKDH. Prevention of Hydrogen Embrittlement in Steels. ISIJ International 2016;56:24–36. https://doi.org/10.2355/isijinternational.ISIJINT-2015-430.

[3] Novak P, Yuan R, Somerday BP, Sofronis P, Ritchie RO. A statistical, physical-based, micro-mechanical model of hydrogen-induced intergranular fracture in steel. J Mech Phys Solids 2010;58:206–26. https://doi.org/10.1016/j.jmps.2009.10.005.

[4] Nibur KA, Somerday BP, Marchi CS, Foulk JW, Dadfarnia M, Sofronis P. The Relationship Between Crack-Tip Strain and Subcritical Cracking Thresholds for Steels in High-Pressure Hydrogen Gas. Metallurgical and Materials Transactions A 2012;44:248–69. https://doi.org/10.1007/s11661-012-1400-5.

[5] Shibata A, Yonemura T, Momotani Y, Park M heom, Takagi S, Madi Y, et al. Effects of local

stress, strain, and hydrogen content on hydrogen-related fracture behavior in low-carbon martensitic steel. Acta Mater 2021;210:116828. https://doi.org/10.1016/j.actamat.2021.116828.
[6] Nagao A, Smith CD, Dadfarnia M, Sofronis P, Robertson IM. The role of hydrogen in hydrogen embrittlement fracture of lath martensitic steel. Acta Mater 2012;60:5182–9. https://doi.org/10.1016/j.actamat.2012.06.040.
[7] Setoyama A, Ogawa Y, Nakamura M, Tanaka Y, Chen T, Koyama M, et al. Transition mechanism of cycle- to time-dependent acceleration of fatigue crack-growth in 0.4 %C Cr-Mo steel in a pressurized gaseous hydrogen environment. Int J Fatigue 2022;163:107039. https://doi.org/10.1016/j.ijfatigue.2022.107039.
[8] Matsuoka S, Matsunaga H, Yamabe J, Hamada S, Iijima T. Various strength properties of SCM435 and SNCM439 low-alloy steels in 115 MPa hydrogen gas and proposal of design guideline. Transactions of the JSME (in Japanese) 2017;83:17-00264-17–00264. https://doi.org/10.1299/transjsme.17-00264.
[9] San Marchi C, Somerday BP. Technical Reference for Hydrogen Compatibility of Materials. 2012.
[10] Sun Z, Benoit G, Moriconi C, Hamon F, Halm D, Hamon F, et al. Fatigue crack propagation under gaseous hydrogen in a precipitation-hardened martensitic stainless steel. Int J Hydrogen Energy 2011;36:8641–4. https://doi.org/10.1016/j.ijhydene.2011.04.094.
[11] Morito S, Yoshida H, Maki T, Huang X. Effect of block size on the strength of lath martensite in low carbon steels. Materials Science and Engineering: A 2006;438–440:237–40. https://doi.org/10.1016/j.msea.2005.12.048.
[12] Du C, Hoefnagels JPM, Vaes R, Geers MGD. Block and sub-block boundary strengthening in lath martensite. Scr Mater 2016;116:117–21. https://doi.org/10.1016/j.scriptamat.2016.01.043.
[13] Galindo-Nava EI, Rivera-Díaz-del-Castillo PEJ. A model for the microstructure behaviour and strength evolution in lath martensite. Acta Mater 2015;98:81–93. https://doi.org/10.1016/j.actamat.2015.07.018.
[14] Tomita Y, Okabayashi K. Effect of microstructure on strength and toughness of heat-treated low alloy structural steels. Metallurgical Transactions A 1986;17:1203–9. https://doi.org/10.1007/BF02665319.
[15] Krauss G. Steels -Processing, Structure, and Performances- 2nd edition. Materials Park, Ohio: ASM International; 2015.
[16] Morito S, Tanaka H, Konishi R, Furuhara T, Maki T. The morphology and crystallography of lath martensite in Fe-C alloys. Acta Mater 2003;51:1789–99. https://doi.org/10.1016/S1359-6454(02)00577-3.
[17] Celada-Casero C, Sietsma J, Santofimia MJ. The role of the austenite grain size in the martensitic transformation in low carbon steels. Mater Des 2019;167:107625. https://doi.org/10.1016/j.matdes.2019.107625.
[18] Morito S, Saito H, Ogawa T, Furuhara T, Maki T. Effect of Austenite Grain Size on the Morphology and Crystallography of Lath Martensite in Low Carbon Steels. ISIJ International 2005;45:91–4. https://doi.org/10.2355/isijinternational.45.91.
[19] Maki T, Tsuzaki K, Tamura I. The Morphology of Microstructure Composed of Lath Martensites in Steels. Transactions of the Iron and Steel Institute of Japan 1980;20:207–14. https://doi.org/10.2355/isijinternational1966.20.207.
[20] Wang C, Wang M, Shi J, Hui W, Dong H. Effect of microstructural refinement on the toughness of low carbon martensitic steel. Scr Mater 2008;58:492–5. https://doi.org/10.1016/j.scriptamat.2007.10.053.
[21] Khan SA, Islam MA. Influence of Prior Austenite Grain Size on the Degree of Temper Embrittlement in Cr-Mo Steel. J Mater Eng Perform 2007;16:80–5. https://doi.org/10.1007/s11665-006-9012-0.
[22] Fuchigami H, Minami H, Nagumo M. Effect of grain size on the susceptibility of martensitic steel to hydrogen-related failure. Philos Mag Lett 2006;86:21–9. https://doi.org/10.1080/09500830500482316.
[23] Takasawa K, Ikeda R, Ishikawa N, Ishigaki R. Effects of grain size and dislocation density

on the susceptibility to high-pressure hydrogen environment embrittlement of high-strength low-alloy steels. Int J Hydrogen Energy 2012;37:2669–75. https://doi.org/10.1016/j.ijhydene.2011.10.099.
[24] Cho L, Bradley PE, Lauria DS, Connolly MJ, Seo EJ, Findley KO, et al. Effects of hydrogen pressure and prior austenite grain size on the hydrogen embrittlement characteristics of a press-hardened martensitic steel. Int J Hydrogen Energy 2021;46:24425–39. https://doi.org/10.1016/j.ijhydene.2021.05.005.
[25] Lessar JF, Gerberich WW. Grain Size Effects in Hydrogen-Assisted Cracking. Metallurgical Transactions A 1976;7:953–60. https://doi.org/10.1007/BF02644060.
[26] Nakamura M, Furubayashi E. Effect of grain size on crack propagation of high strength steel in gaseous hydrogen atmosphere. Materials Science and Technology 1990;6:604–10. https://doi.org/10.1179/mst.1990.6.7.604.
[27] Ogawa Y, Iwata K. Resistance of pearlite against hydrogen-assisted fatigue crack growth. Int J Hydrogen Energy 2022;47:31703–8. https://doi.org/10.1016/j.ijhydene.2022.07.074.
[28] Sun Z, Moriconi C, Benoit G, Halm D, Henaff G. Fatigue Crack Growth under High Pressure of Gaseous Hydrogen in a 15-5PH Martensitic Stainless Steel: Influence of Pressure and Loading Frequency. Metallurgical and Materials Transactions A 2013;44:1320–30. https://doi.org/10.1007/s11661-012-1133-5.
[29] Suresh S, Ritchie RO. Mechanistic dissimilarities between environmentally influenced fatigue-crack propagation at near-threshold and higher growth rates in lower strength steels. Metal Science 1982;16:529–38. https://doi.org/10.1179/msc.1982.16.11.529.
[30] Briottet L, Moro I, Escot M, Furtado J, Bortot P, Tamponi GM, et al. Fatigue crack initiation and growth in a CrMo steel under hydrogen pressure. Int J Hydrogen Energy 2015;40:17021–30. https://doi.org/10.1016/j.ijhydene.2015.05.080.
[31] Matsuoka S, Takakuwa O, Okazaki S, Yoshikawa M, Yamabe J, Matsunaga H. Peculiar temperature dependence of hydrogen-enhanced fatigue crack growth of low-carbon steel in gaseous hydrogen. Scr Mater 2018;154:101–5. https://doi.org/10.1016/j.scriptamat.2018.05.035.
[32] Ogawa Y, Umakoshi K, Nakamura M, Takakuwa O, Matsunaga H. Hydrogen-assisted, intergranular, fatigue crack-growth in ferritic iron: Influences of hydrogen-gas pressure and temperature variation. Int J Fatigue 2020;140:105806. https://doi.org/10.1016/j.ijfatigue.2020.105806.
[33] Grange RA. The rapid heat treatment of steel. Metallurgical Transactions 1971;2:65–78. https://doi.org/10.1007/BF02662639.
[34] Furuhara T, Kikumoto K, Saito H, Sekine T, Ogawa T, Morito S, et al. Phase Transformation from Fine-grained Austenite. ISIJ International 2008;48:1038–45. https://doi.org/10.2355/isijinternational.48.1038.
[35] Hidalgo J, Santofimia MJ. Effect of Prior Austenite Grain Size Refinement by Thermal Cycling on the Microstructural Features of As-Quenched Lath Martensite. Metallurgical and Materials Transactions A 2016;47:5288–301. https://doi.org/10.1007/s11661-016-3525-4.
[36] ASTM E647−13. Standard Test Method for Measurement of Fatigue Crack Growth Rates. American Society for Testing and Materials 2014:1–50. https://doi.org/10.1520/E0647-13E01.2.
[37] Ogawa Y, Iwata K. Fatigue crack propagation in pearlitic steel under pressurized gaseous hydrogen: influences of microstructure size and strength level. ISIJ International 2023:ISIJINT-2023-011. https://doi.org/10.2355/isijinternational.ISIJINT-2023-011.
[38] Ogawa K, Matsumoto Y, Suzuki H, Takai K. Hydrogen Embrittlement Susceptibility Evaluation of Tempered Martensitic Steels Showing Different Fracture Surface Morphologies. ISIJ International 2019;59:1705–14. https://doi.org/10.2355/isijinternational.ISIJINT-2019-130.
[39] Chen T, Chiba T, Koyama M, Akiyama E, Takai K. Factors Distinguishing Hydrogen-Assisted Intergranular and Intergranular-Like Fractures in a Tempered Lath Martensitic Steel. Metallurgical and Materials Transactions A 2022;53:1645–58. https://doi.org/10.1007/s11661-022-06608-2.
[40] Chen T, Chiba T, Koyama M, Shibata A, Akiyama E, Takai K. Hierarchical Characteristics of

Hydrogen-Assisted Crack Growth and Microstructural Strain Evolution in Tempered Martensitic Steels: Case of Quasi-cleavage Fracture. Metallurgical and Materials Transactions A 2021;52:4703–13. https://doi.org/10.1007/s11661-021-06423-1.
[41] Chen T, Koyama M, Ogawa Y, Matsunaga H, Akiyama E. Martensite Boundary Characteristics on Cycle- and Time-Dependent Fatigue Crack Growth Paths of Tempered Lath Martensitic Steels in a 90 MPa Gaseous Hydrogen Atmosphere. Metallurgical and Materials Transactions A 2023. https://doi.org/10.1007/s11661-023-07041-9.
[42] Yamaguchi M, Ebihara K-I, Itakura M, Kadoyoshi T, Suzudo T, Kaburaki H. First-Principles Study on the Grain Boundary Embrittlement of Metals by Solute Segregation: Part II. Metal (Fe, Al, Cu)-Hydrogen (H) Systems. Metallurgical and Materials Transactions A 2011;42:330–9. https://doi.org/10.1007/s11661-010-0380-6.
[43] Nagao A, Dadfarnia M, Somerday BP, Sofronis P, Ritchie RO. Hydrogen-enhanced-plasticity mediated decohesion for hydrogen-induced intergranular and “quasi-cleavage” fracture of lath martensitic steels. J Mech Phys Solids 2018;112:403–30. https://doi.org/10.1016/j.jmps.2017.12.016.
[44] Oriani RA, Josephic PH. Equilibrium aspects of hydrogen-induced cracking of steels. Acta Metallurgica 1974;22:1065–74. https://doi.org/10.1016/0001-6160(74)90061-3.
[45] Wang S, Martin ML, Sofronis P, Ohnuki S, Hashimoto N, Robertson IM. Hydrogen-induced intergranular failure of iron. Acta Mater 2014;69:275–82. https://doi.org/10.1016/j.actamat.2014.01.060.
[46] Koyama M, Habib K, Masumura T, Tsuchiyama T, Noguchi H. Gaseous hydrogen embrittlement of a Ni-free austenitic stainless steel containing 1 mass% nitrogen: Effects of nitrogen-enhanced dislocation planarity. Int J Hydrogen Energy 2020;45:10209–18. https://doi.org/10.1016/j.ijhydene.2020.02.014.
[47] Robertson IM, Sofronis P, Nagao A, Martin ML, Wang S, Gross DW, et al. Hydrogen Embrittlement Understood. Metallurgical and Materials Transactions B 2015;46:1085–103. https://doi.org/10.1007/s11663-015-0325-y.
[48] Momotani Y, Shibata A, Yonemura T, Bai Y, Tsuji N. Effect of initial dislocation density on hydrogen accumulation behavior in martensitic steel. Scr Mater 2020;178:318–23. https://doi.org/10.1016/j.scriptamat.2019.11.051.
[49] Song EJ, Wang Y, Feng Z, Wu Z, Amaro R, Slifka A, et al. Correlating Steel Pipeline Microstructure to Fatigue Crack Growth Rates in High Pressure Hydrogen Gas. Albuquerque, NM: 2017. https://doi.org/SAND2017-11885C.
[50] Suresh S. Crack deflection: Implications for the growth of long and short fatigue cracks. Metallurgical Transactions A 1983;14:2375–85. https://doi.org/10.1007/BF02663313.
[51] Suresh S, Ritchie RO. A geometric model for fatigue crack closure induced by fracture surface roughness. Metallurgical Transactions A 1982;13:1627–31. https://doi.org/10.1007/BF02644803.
[52] Shibata A, Momotani Y, Murata T, Matsuoka T, Tsuboi M, Tsuji N. Microstructural and crystallographic features of hydrogen-related fracture in lath martensitic steels. Materials Science and Technology 2017;33:1524–32. https://doi.org/10.1080/02670836.2017.1312210.
[53] Okada K, Shibata A, Gong W, Tsuji N. Effect of hydrogen on evolution of deformation microstructure in low-carbon steel with ferrite microstructure. Acta Mater 2022;225:117549. https://doi.org/10.1016/j.actamat.2021.117549.
[54] Gilman JJ. Reduction of Cohesion in Ionic Crystals by Dislocations. J Appl Phys 1961;32:738–9. https://doi.org/10.1063/1.1736081.
[55] Wiederhorn S. Elastic Energy Release from Slip Bands During Fracture. J Appl Phys 1962;33:3233–4. https://doi.org/10.1063/1.1931143.
[56] Ryou KH, Nambu S, Koseki T. Effect of carbon content on selection of slip system during uniaxial tensile deformation of lath martensite. Materials Science and Engineering: A 2020;777:139090. https://doi.org/10.1016/j.msea.2020.139090.
[57] Tanaka Y, Takaki S, Tsuchiyama T, Uemori R. Effect of Grain Size on the Yield Stress of Cold Worked Iron. ISIJ International 2018;58:1927–33. https://doi.org/10.2355/isijinternational.ISIJINT-2018-371.
[58] Ashby MF. The deformation of plastically non-homogeneous materials. The Philosophical

Magazine: A Journal of Theoretical Experimental and Applied Physics 1970;21:399–424. https://doi.org/10.1080/14786437008238426.
[59] Anderson TL. Fracture mechanics fundamentals and applications. CRC Press 2017.
[60] Roven HJ, Nes E. Cyclic deformation of ferritic steel—II. Stage II crack propagation. Acta Metallurgica et Materialia 1991;39:1735–54. https://doi.org/10.1016/0956-7151(91)90142-N.